

**FABRICATION AND CHARACTERIZATION OF
POLYMERIC AND NANOSTRUCTURED
CARBON NITRIDE THIN FILMS:
A SIMPLE DIFFERENCE IN ELECTRODE DISTANCE**

RICHARD ANAK RITIKOS

**FACULTY OF SCIENCE
UNIVERSITY OF MALAYA
KUALA LUMPUR**

2011

**FABRICATION AND CHARACTERIZATION OF
POLYMERIC AND NANOSTRUCTURED
CARBON NITRIDE THIN FILMS:
A SIMPLE DIFFERENCE IN ELECTRODE DISTANCE**

RICHARD ANAK RITIKOS

**THESIS SUBMITTED IN FULFILMENT OF
THE REQUIREMENTS FOR THE DEGREE OF
DOCTOR OF PHILOSOPHY**

**DEPARTMENT OF PHYSICS
FACULTY OF SCIENCE
UNIVERSITY OF MALAYA
KUALA LUMPUR**

2011

UNIVERSITI MALAYA

ORIGINAL LITERARY WORK DECLARATION

Name of Candidate: RICHARD ANAK RITIKOS (I.C/Passport No: 740812135239)

Registration/Matric No: SHC050028

Name of Degree: DOCTOR OF PHILOSOPHY

Title of Project Paper/Research Report/Dissertation/Thesis ("this Work"):

FABRICATION AND CHARACTERIZATION OF POLYMERIC AND
NANOSTRUCTURED CARBON NITRIDE THIN FILMS:
A SIMPLE DIFFERENCE IN ELECTRODE DISTANCE

Field of Study:

LOW DIMENSIONAL MATERIALS

I do solemnly and sincerely declare that:

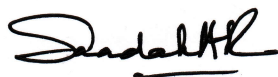
- (1) I am the sole author/writer of this Work;
- (2) This Work is original;
- (3) Any use of any work in which copyright exists was done by way of fair dealing and for permitted purposes and any excerpt or extract from, or reference to or reproduction of any copyright work has been disclosed expressly and sufficiently and the title of the Work and its authorship have been acknowledged in this Work;
- (4) I do not have any actual knowledge nor do I ought reasonably to know that the making of this work constitutes an infringement of any copyright work;
- (5) I hereby assign all and every rights in the copyright to this Work to the University of Malaya ("UM"), who henceforth shall be owner of the copyright in this Work and that any reproduction or use in any form or by any means whatsoever is prohibited without the written consent of UM having been first had and obtained;
- (6) I am fully aware that if in the course of making this Work I have infringed any copyright whether intentionally or otherwise, I may be subject to legal action or any other action as may be determined by UM.



Candidate's Signature

Date 30/11/2011

Subscribed and solemnly declared before,



Witness's Signature

Date 30/11/11

Name: **Profesor Dr. Saadah Abdul Rahman**
Designation: **Jabatan Fizik**
Universiti Malaya
50603 Kuala Lumpur

ABSTRACT

This work gives an insight on the fabrication and characterization of two distinctly different hydrogenated carbon nitride $\text{CN}_x\text{:H}$ structured films showing either polymeric, p- $\text{CN}_x\text{:H}$ or nanostructured, ns- $\text{CN}_x\text{:H}$ film growth. These structures were obtained using radio frequency (rf) plasma enhanced chemical vapour deposition employing a parallel-plate electrode configuration, under the same deposition parameters except for the change in the electrode distance. It was this simple change in the distance which induced the structural transformation from p- $\text{CN}_x\text{:H}$ films obtained at distance of six to three cm, to the ns- $\text{CN}_x\text{:H}$ films produced at two to one cm. Each type of film showed its own unique characteristics. For the p- $\text{CN}_x\text{:H}$ films deposited at an electrode distance of 5 cm, their PL spectra showed two main peaks assumed to be attributed to the presence of sp^2 clusters and nitrogen bonding in the films. Further studies showed that the optimized rf power and nitrogen-to-methane $\text{N}_2\text{:CH}_4$ gas-flow-rate ratio to obtain p- $\text{CN}_x\text{:H}$ films with the highest PL intensities were 80 W and 0.70, respectively. There appeared to be no direct correlation between the PL properties and optical energy gap. However, the PL characteristics were dependent on the N content in the films. From extensive bonding studies carried out on these films, it was found that N is incorporated most significantly through nitrile, isonitrile and $\text{sp}^2\text{-C=N}$ bonding configurations. Also, these films were thermally stable when annealed in nitrogen up to temperatures of 500 °C, though the PL intensities start to decline even from 200 °C. The recombination centers which produced these high PL intensities were attributed to the CH_n , C=N and the isolated and/or fused aromatic rings bonded to nitrile ($-\text{C}\equiv\text{N}$) which may contribute significantly as recombination centers.

While the studies of p- $\text{CN}_x\text{:H}$ films were focused on their PL characteristics, a more fundamental approach was taken in the study of ns- $\text{CN}_x\text{:H}$. These novel ns- $\text{CN}_x\text{:H}$ films were obtained at low deposition temperatures without the use of metal-catalyst or template, and could be grown directly on the bare silicon and quartz substrates. The focus of the study of these ns- $\text{CN}_x\text{:H}$ films was on the formation of vertically aligned $\text{CN}_x\text{:H}$ nanorods and their growth mechanism. The optimized parameters for the formation these nanorods were determined to be at P_{rf} of 80 W and $\text{N}_2\text{:CH}_4$ ratio of 0.70. This coincided with the maximum N content and preferential bonding of isonitrile bonded to fused or isolated aromatic rings in the films. These nanorods were made up of C nanographitic sp^2 clusters embedded in a carbon-nitrogen amorphous matrix which surrounded, encapsulated and held them together. The growth mechanism of these vertically aligned nanorods was proposed.

In the optimization studies of both materials, one fascinating conclusion was uncovered. The optimized deposition parameters for both exceptional characteristics of these structured films were the same. It is the simply the difference in electrode distance at these optimal P_{rf} and $\text{N}_2\text{:CH}_4$ ratio, which induces the formation of these two significantly different structured films.

ABSTRAK

Kerja penyelidikan ini memberi pemahaman yang mendalam terhadap fabrikasi dan pencirian dua jenis karbon nitrida berhidrogen ($CN_x:H$) yang jelas berbeza dari segi struktur filemnya samaada filem polimerik ($p-CN_x:H$) atau berstruktur nano ($ns-CN_x:H$). Struktur-struktur ini telah diperolehi dengan menggunakan kaedah pemendapan frekuensi radio wap kimia secara peningkatan plasma dengan konfigurasi kepingan elektrod selari, dimana parameter pemendapan yang digunakan adalah sama kecuali beza jarak diantara elektrod. Perubahan jarak ini dengan mudahnya mendorong transformasi struktur filem dari $p-CN_x:H$ yang diperolehi pada jarak enam hingga tiga cm kepada filem $ns-CN_x:H$ yang dihasilkan pada jarak dua hingga satu cm. Kedua-dua jenis filem menunjukkan ciri-ciri unik yang tersendiri. Bagi filem $p-CN_x:H$ yang dimendapkan pada jarak elektrod lima cm, spectra PL menunjukkan dua puncak utama yang dipercayai berkait rapat dengan kehadiran kelompok-kelompok sp^2 dan ikatan nitrogen dalam filem-filem tersebut. Kajian lanjut menunjukkan kuasa rf (K_{rf}) dan kadar nisbah campuran aliran gas nitrogen terhadap gas metana ($N_2:CH_4$) yang optima bagi menghasilkan filem $p-CN_x:H$ dengan PL yang berkeamatan paling tinggi masing-masing adalah 80W dan 0.70. Didapati tiada hubungan terus diantara sifat PL dan jurang tenaga optikal. Walaubagaimanapun, sifat PL bergantung kepada kandungan N dalam filem-filem tersebut. Melalui kajian ikatan kimia yang terperinci, didapati penggabungan N yang sangat penting berlaku melalui konfigurasi ikatan nitrile, isonitrile dan $sp^2-C=N$. Didapati juga, filem-filem ini stabil sehingga suhu 500 °C walaupun keamatan PLnya menurun seawal suhu 200 °C. Pusat penggabungan semula yang menghasilkan keamatan PL yang tinggi dikaitkan dengan kehadiran CH_n , $C=N$ dan nitrile ($-C\equiv N$) yang terikat kepada lingkaran aromatik yang terpencil dan/atau terpadu yang mungkin merupakan penyumbang terpenting sebagai pusat-pusat penggabungan semula.

Berbeza dengan kajian terhadap filem $p-CN_x:H$ yang tertumpu kepada sifat-sifat PL, pendekatan yang lebih asas telah diambil dalam kajian terhadap $ns-CN_x:H$. Filem-filem $ns-CN_x:H$ yang belum pernah dikaji ini telah di perolehi pada suhu pemendapan yang rendah tanpa menggunakan pemangkin logam atau templit dan boleh dimendap secara terus di atas substrak silikon dan kuarza yang terdedah. Kajian terhadap filem-filem $ns-CN_x:H$ ini adalah tertumpu kepada pembentukan filem rod-nano $CN_x:H$ yang tegak menjajar serta mekanisma pertumbuhannya. Parameter optima bagi menghasilkan rod-nano ini adalah K_{rf} bernilai 80 W dan nisbah $N_2:CH_4$ bernilai 0.70. Ini sejajar dengan kandungan maksima N dan kecenderungan ikatan isonitrile yang terikat kepada lingkaran aromatic yang terpencil dan/atau terpadu didalam filem tersebut. Rod nano ini terdiri daripada kelompok C sp^2 nano-grafitik yang terbenam didalam matrik amorfus karbon-nitrogen yang mengelilingi, mengkapsul dan mengikat kelompok-kelompok ini bersama. Mekanisma pertumbuhan rod-nano yang tegak menjajar ini dicadangkan.

Dalam kajian pengoptimaan kedua-dua bahan ini, satu kesimpulan yang menarik didedahkan. Parameter pemendapan optima bagi ciri-ciri unik kedua-dua struktur filem ini adalah sama. Perbezaan jarak antara elektrod pada nilai-nilai optimum P_{rf} dan nisbah $N_2:CH_4$ tersebut yang mendorong pemendapan filem yang jelas perbezaan strukturnya.

ACKNOWLEDGEMENTS

First and foremost, I would like to thank God for all the blessings I have received throughout the years leading to this day. For the gift of my dear wife and wonderful son, for my supporting families (in-laws included) and many friends, for my supervisors and lecturers and many others who have come along the way to lend a hand. I lovingly and fearfully thank God for them.

I would like to express my sincere gratitude to my supervisors, Professor Datin Dr. Saadah Abdul Rahman and Associate Professor Dr. Siti Meriam Ab. Gani, for their guidance, encouragement and freedom to explore some of my own ideas during this PhD work. Thank you for being more than my supervisors but also a friend to my family and I. My gratitude also goes to the lecturers of Low Dimensional Materials Research Center, especially Professor Datuk Muhamad Rasat Muhamad, the laboratory assistants, Pn. Norlela Mohd Shahardin and En. Mohamad Aruf, and all members of the Department of Physics, University of Malaya for their kind support, assistance, friendship and guidance. And of course, to Ms. Nur Maisarah Abdul Rashid, Ms. Noor Hamizah Khanis and Ms. Maisara Othman, who are continuing this work I have started and who have always been willing to extend a helping hand whenever I was just too tired, busy or lazy. Thanks girls!!! Not forgetting my colleagues, in particular Mr. Goh Boon Tong, Mr. Gan Wee Chen and Dr. Thamilselvi for making the laboratory such a fun and crazy place to work in. I hope this will not be the end, but a start of many great studies and collaboration works.

I would like to thank University of Malaya and Malaysian Ministry of Higher Education (MoHE) for awarding the SLAI scholarship scheme to pursue this PhD. I would also like to acknowledge the financial supports given, which include IRPA 09-02-03-0222-EA222, the Short-Term Grants PJP FS282-2007C and FS290-2008C, University Research grant RG064-09AFR, Fundamental Research Grants FP016/2008C and FP052/2010B and the Brain Gain Malaysia Program. Also, I am really grateful to our collaborator, Professor Dr. Yoke Khin Yap of Michigan Technological University, USA for the invaluable discussions and advice on this work.

My heart-felt gratitude and love goes to my families, especially my parents, Mr. Ritikos Jitab and Mdm. Mary Jandom Anak Nangod, for all the love, support and prayers. Thank you, Papa and Mama for waiting in anticipation and prayer for me to get my “Dr” title and for being the motivation in my life to study to the highest level. With this, I hope one of the dreams in your life to have a Dr in the family is fulfilled.

Last but not the least (maybe even the most important...) I thank my beautiful wife, Elaine Marcia Wong, and wonderful son, Mark Isaac Ritikos, for making working, meaningful and being at home, wonderful. Thank you for being the greatest motivation in my life. This thesis is dedicated to you both...

LIST OF PUBLICATIONS

REVIEWED PAPERS

Chapter 6: Section 6.4 and 6.5

1. **Catalyst-free formation of vertically-aligned carbon nanorods as induced by nitrogen incorporation**

Carbon, Volume 49, Issue 6, Pages 1842-1848, May 2011

Ritikos, R., Rahman, S.A., Gani, S.M.A., Muhamad, M.R., Yap, Y.K.

ISI: Impact factor 4.896. Category: Q1

Chapter 5: Section 5.4

2. **Effect of annealing on the optical and chemical bonding properties of hydrogenated amorphous carbon and hydrogenated amorphous carbon nitride thin films**

Japanese Journal of Applied Physics, Volume 48, Issue 10 Part 1, Pages 1013011-1013014, December 2009

Ritikos, R., Siong, C.C., Gani, S.M.A., Muhamad, M.R., Rahman, S.A.

ISI: Impact factor 1.024. Category: Q3

Chapter 5: Section 5.3

3. **Influence of Nitrogen/Methane ratio on the properties of hydrogenated amorphous carbon nitride deposited by r.f. PECVD technique**

AIP Conference Proceedings, Volume 1150, Pages 266-269, November 2009

Ritikos, R., Meriam Ab. Gani, S., Aspanut, Z., Abd. Rahman, S.

ISI Proceeding paper

Chapter 5: Section 5.2

4. **Dependence of radio frequency power on optical, chemical bonding and photoluminescence properties of hydrogenated amorphous carbon nitride films**

IEEE International Conference on Semiconductor Electronics, Proceedings, ICSE, Pages 781-785, December 2006

Ritikos, R., Tong, G.B., Awang, R., Gani, S.M.A., Rahman, S.A.

Scopus

OTHER RELATED PUBLICATIONS

On aspects of applications

1. **Highly reflective nc-Si:H/a-CN_x:H multilayer films prepared by r.f. PECVD technique**

Thin Solid Films, Volume 517, Issue 17, Pages 5092-5095, July 2009

Ritikos, R., Goh, B.T., Sharif, K.A.M., Muhamad, M.R., Rahman, S.A.

ISI: Impact factor 1.935. Category: Q1

- On aspects of CH₄+N₂+H₂ precursor mixtures
2. **Effects of rf power on the structural properties of carbon nitride thin films prepared by plasma enhanced chemical vapour deposition**
Thin Solid Films, Volume 519, Issue 15, Pages 4981-4986, May 2011
 Othman, M., Ritikos, R., Khanis, N.H., Rashid, N.M.A., Rahman, S.A., Gani, S.M.A., Muhamad, M.R.
 ISI: Impact factor 1.935. Category: Q1
- On aspects of modifications of ns-CN_x:H growth (as an extension of this work)
3. **Effect of pre-deposited carbon layer on the formation of carbon nitride nanostructures prepared by radio-frequency plasma enhanced chemical vapour deposition**
Materials Chemistry and Physics, Volume 130, Issues 1-2, Pages 218-222
 October 2011
 Khanis, N.H., Ritikos, R., Othman, M., Rashid, N.M.A., Gani, S.M.A., Muhamad, M.R., Rahman S.A.,
 ISI: impact factor 2.356. Category: Q1
- On aspects of deposition duration for p-CN_x:H films
4. **Studies on optical and photoluminescence properties of a-CN_x thin films**
Materials Research Innovations, Volume 13, Issue 3, Pages 168-170, September 2009
 Rahman, Z.A., Ritikos, R., Rahman, S.A.
 ISI: Impact factor 0.638. Category: Q3
- On aspects of a-C:H films
5. **The effects of deposition pressure on the optical and structural properties of d.c. PECVD hydrogenated amorphous carbon films**
Materials Science Forum, Volume 517, Pages 81-84, December 2006
 Awang, R., Tong, G.B., Gani, S.M.Ab., Ritikos, R., Rahman, S.A.
 Scopus

PAPERS IN WRITING

- Chapter 4
- 1 **Transformation of carbon nitride thin films into vertically-aligned nanorods**
Ritikos, R., Rahman, S.A., Gani, S.M.A., Muhamad, M.R., Yap Y.K.,
 To be submitted to *Acta Materialia* for reviewing
 (ISI: impact factor 3.781. Category: Q1)
- Chapter 6: Section 6.3
- 2 **Influence of Nitrogen Incorporation for the Catalyst-free Synthesis of Vertically-aligned Nitrogen Doped Carbon Nanostructures** (unedited title)
 Richard Ritikos, Yoke Khin Yap, Muhamad Rasat Muhamad, Siti Meriam Ab. Gani and Saadah Abdul Rahman
 Paper in writing

On different gas (ethane and nitrogen) mixture as precursors

- 3 **Effects of N₂ flow-rate on the properties of CN_x thin films prepared by rf PECVD from ethane and nitrogen**

Othman, M., Ritikos, R., Khanis, N.H., Rashid, N.M.A., Rahman, S.A., Gani, S.M.A., Muhamad, M.R.

Paper in writing

On aspects of applications

- 4 **Effects of thermal annealing on the properties of highly reflective nc-Si:H/a-CN_x:H multilayered films prepared by r. f. PECVD technique**

Rashid, N.M.A., Ritikos, R., Goh, B.T., Gani, S.M.A., Muhamad M.R., Rahman S.A.,

Paper in writing

TABLE OF CONTENTS

	Page
Declaration	ii
Abstract	iii
Abstrak	iv
Acknowledgements	v
List of Publications	vi
Table of Contents	ix
List of Figures	xv
List of Tables	xxv
1 INTRODUCTION	
1.1 From Carbon to Carbon Nitride: A Progression in Research	1
1.2 Nitrogen Incorporation into Carbon Films: Advantages and Applications	7
1.3 Aspects, Motivation and Objectives for This Study	10
1.4 Outline of Thesis	12
2 LITERATURE REVIEW	
2.1 Introduction	15
2.2 Review on Common Deposition Techniques for Carbon Nitride films	15
2.2.1 <i>Laser Ablation</i>	16
2.2.2 <i>Sputtering</i>	18
2.2.3 <i>Chemical vapour deposition</i>	21
2.2.3.1 <i>Hot-wire or hot-filament chemical vapour deposition</i>	22

2.2.3.2	<i>Thermal chemical vapour deposition.....</i>	24
2.2.3.3	<i>Microwave plasma enhanced chemical vapour deposition.....</i>	25
2.2.3.4	<i>Electron cyclotron chemical vapour deposition.....</i>	27
2.2.3.5	<i>Radio frequency plasma enhanced chemical vapour deposition.....</i>	29
2.3	Choice of Deposition Technique.....	32
2.4	Review on Analytical Methods.....	33
2.4.1	<i>Optical properties.....</i>	34
2.4.2	<i>Raman spectroscopic studies on carbon nitride thin films.....</i>	36
2.4.3	<i>Fourier transform infrared spectroscopy.....</i>	40
2.4.4	<i>Photoluminescence properties of carbon nitride thin films.....</i>	43
3	EXPERIMENTAL AND ANALYTICAL METHOD	
3.1	Introduction.....	48
3.2	Sample Preparation.....	49
3.2.1	<i>Overview on radio frequency plasma enhanced chemical vapour deposition.....</i>	49
3.2.2	<i>Substrate cleaning procedure.....</i>	52
3.2.3	<i>Thin film deposition.....</i>	53
3.3	Thermal Annealing.....	57
3.4	Characterization and Analytical procedures.....	58
3.4.1	<i>Determination of growth rate measured by surface profilometry.....</i>	59
3.4.2	<i>Optical properties measured by ultra violet visible near infrared spectroscopy.....</i>	61
3.4.3	<i>Photoluminescence properties measured using photoluminescence pectroscopy.....</i>	66

3.4.4	<i>Elemental composition determined by Auger electron spectroscopy</i>	68
3.4.5	<i>Structural characteristics determined by Raman scattering spectroscopy</i>	70
3.4.6	<i>Chemical bonding studies via Fourier transform infrared spectroscopy</i>	71
3.4.7	<i>High resolution surface and cross-sectional images obtained using field emission scanning electron microscopy</i>	75
3.4.8	<i>Atomic resolution images obtained using high resolution transmission electron microscopy</i>	76
4	FROM POLYMERIC TO NANOSTRUCTURED CARBON NITRIDE THIN FILMS: A STUDY OF ELECTRODE DISTANCE	
4.1	Introduction and Overview	78
4.2	Deposition Parameter	79
4.3	Experimental Results	80
4.3.1	<i>Field emission scanning electron microscopy (FESEM)</i>	80
4.3.2	<i>Auger electron spectroscopy</i>	85
4.3.3	<i>Raman scattering</i>	87
4.3.4	<i>Fourier transform infrared spectroscopy (FTIR)</i>	93
4.3.5	<i>Optical spectroscopy</i>	98
4.3.6	<i>Photoluminescence spectroscopy</i>	102
4.4	Summary	105
5	FORMATION OF POLYMERIC HYDROGENATED CARBON NITRIDE FILMS	
5.1	Introduction	108
5.1.1	<i>Growth mechanism postulated</i>	110

5.2	Effects of Radio-Frequency Power on the Properties of Polymeric $CN_x:H$	116
5.2.1	<i>Determination of growth rate measured by surface profilometry</i>	118
5.2.2	<i>Optical properties measured by UV-Vis NIR spectroscopy</i>	118
5.2.3	<i>Photoluminescence properties</i>	120
5.2.4	<i>Elemental composition determined by Auger electron spectroscopy (AES)</i>	123
5.2.5	<i>Structural characteristics determined by Raman spectroscopy</i>	125
5.2.6	<i>Chemical bonding studies via Fourier transform infrared spectroscopy</i>	128
5.3	Effects of Nitrogen-to-methane Gas Flow-Rate Ratio on the Properties of Polymeric $CN_x:H$	133
5.3.1	<i>Determination of growth rate measured by surface profilometry</i>	135
5.3.2	<i>Optical properties measured by UV-Vis NIR spectroscopy</i>	135
5.3.3	<i>Photoluminescence properties</i>	136
5.3.4	<i>Elemental composition determined by Auger electron spectroscopy (AES)</i>	139
5.3.5	<i>Structural characteristics determined by Raman scattering spectroscopy</i>	140
5.3.6	<i>Chemical bonding studies via Fourier transform infrared spectroscopy</i>	142
5.4	Effects of Thermal Annealing on the Properties of Polymeric $CN_x:H$	150
5.4.1	<i>Thickness variation measured by surface profilometry</i>	152
5.4.2	<i>Chemical bonding studies via Fourier transform infrared spectroscopy</i>	153
5.4.3	<i>Optical properties measured by UV-Vis NIR spectroscopy</i>	158
5.4.4	<i>Elemental composition determined by Auger electron spectroscopy (AES)</i>	159

5.4.5	<i>Structural characteristics determined by Raman scattering spectroscopy</i>	160
5.4.6	<i>Photoluminescence properties</i>	163
5.5	Summary	166
6	FORMATION OF HIGHLY VERTICALLY ALIGNED HYDROGENATED CARBON NITRIDE FILMS	
6.1	Introduction	169
6.2	Effects of Applied Radio Frequency Power on the Growth of Nanostructured Hydrogenated Carbon Nitride Films	171
6.2.1	<i>Surface and cross-sectional images obtained using field emission scanning electron microscopy (FESEM)</i>	173
6.2.2	<i>Elemental composition determined by Auger electron spectroscopy (AES)</i>	176
6.2.3	<i>Structural characteristics determined by Raman scattering spectroscopy</i>	177
6.2.4	<i>Chemical bonding studies via Fourier transform infrared spectroscopy (FTIR)</i>	181
6.3	Effects of Nitrogen-to-methane Gas Flow-Rate Ratio on the Growth of Nanostructured Hydrogenated Carbon Nitride Films	188
6.3.1	<i>Surface and cross-sectional images obtained using field emission scanning electron microscopy (FESEM)</i>	190
6.3.2	<i>Elemental composition determined by Auger electron spectroscopy (AES)</i>	192
6.3.3	<i>Structural characteristics determined by Raman scattering spectroscopy</i>	193
6.3.4	<i>Chemical bonding studies via Fourier transform infrared spectroscopy (FTIR)</i>	196
6.4	Effects of Deposition Duration on the Growth of Nanostructured Hydrogenated Carbon Nitride Films	203

6.4.1	<i>Surface and cross-sectional images obtained using field emission scanning electron microscopy (FESEM)</i>	205
6.4.2	<i>Elemental composition determined by Auger electron spectroscopy (AES)</i>	207
6.4.3	<i>Structural characteristics determined by Raman scattering spectroscopy</i>	209
6.4.4	<i>Chemical bonding studies via Fourier transform infrared spectroscopy (FTIR)</i>	212
6.4.5	<i>Atomic scale imaging using high resolution transmission electron microscopy (HRTEM)</i>	217
6.5	Growth Mechanism Proposed	219
6.6	Summary	221
7	SUMMARY, CONCLUSION AND SUGGESTIONS FOR FUTURE WORKS	
7.1	Conclusion	223
7.2	Suggestions for Future Works	224
	REFERENCES	226
	APPENDIX 1	244
	APPENDIX 2	245

LIST OF FIGURES

		Page
Figure 1.1	Diagram representation of the timeline in the research of carbon and carbon nitride thin films with critical milestones shown in bold letters followed by some other relevant findings. This information is accurate to the knowledge of the author.	6
Figure 2.1	Schematic diagrams of various configurations of pulsed laser ablation systems	17
Figure 2.2	Schematic diagrams of two configurations of hybrid pulsed laser ablation systems	18
Figure 2.3	Schematic diagrams of different variations of sputtering systems.	20
Figure 2.4	Schematic diagrams of two different variations of HFCVD systems (a) and (b) and a HF – rf PECVD hybrid system (c).	23
Figure 2.5	Schematic diagrams of two different variations of TCVD systems.	24
Figure 2.6	Schematic diagrams of various MWCVD systems.	26
Figure 2.7	Schematic diagrams of different variations of ECRCVD systems.	28
Figure 2.8	Schematic diagrams of two different variations of rf PECVD systems.	30
Figure 2.9	Examples of typical Raman spectra for different carbon film structure at different excitation wavelength. Figures are taken from those illustrated by Chu and Li (Chu and Li 2006)	37
Figure 2.10	Vibration modes for CH ₂ group. (+ and – indicate movement perpendicular to the plane of this page) (Silverstein and Webster 1997)	41
Figure 2.11	Example of typical Fourier transform infrared spectrum for carbon nitride films obtained in this work.	42
Figure 2.12	Schematic diagram of proposed photoluminescence mechanism (Ferrari et al. 2003; Robertson 1997).	45
Figure 3.1	Schematics of rf PECVD setup showing the reaction chamber and corresponding subsystems	50
Figure 3.2	Schematic diagram and picture of home-built rf PECVD.	52
Figure 3.3	Variation in substrate temperature as a function of deposition time at different distance between electrodes.	55

Figure 3.4	KLA-Tencor P-6 surface profilometer used for thickness measurements.	59
Figure 3.5	Variation of profilometer scan for varied applied rf power. Each scan is taken for thickest measured film side.	60
Figure 3.6	Variation of profilometer scan for film deposited at applied rf power of 100W for four different sides of the film area.	61
Figure 3.7	JascoV-570 UV-Vis-NIR spectrophotometer used for optical characterizations.	61
Figure 3.8	Example of optical spectrum showing the envelope method employed on the interference fringes.	63
Figure 3.9	Graph showing a typical refractive index, n versus incident wavelength λ plot calculated from the raw data of UV-Vis-NIR measurement.	64
Figure 3.10	Variation in optical spectra in (a) transmission, (b) reflectance and (c) calculated absorption spectra as a function of electrode distance.	65
Figure 3.11	Jobin Yvon HR 800 UV Raman/photoluminescence photometer used for photoluminescence and structural studies.	67
Figure 3.12	Example of photoluminescence Gaussian fitting for the film deposited at applied rf power of 80W.	68
Figure 3.13	JEOL JAMP-9500F field emission Auger microprobe used for elemental composition measurements	69
Figure 3.14	Example of typical Auger electron spectroscopy measurements showing the Variation in AES spectra as a function of applied rf power.	69
Figure 3.15	Examples of typical Raman scattering spectra with (a) raw data showing baseline fitting and (b) spectra with base line correction showing Gaussian fitting to obtain D and G bands. Examples were taken for as-deposited and thermally annealed carbon nitride films at 700 °C.	71
Figure 3.16	Perkin Elmer System 2000 FTIR used for chemical bonding studies.	72
Figure 3.17	Example of typical Fourier transform infrared spectrum for carbon nitride films	72
Figure 3.18	Example of typical separation of Fourier transform infrared spectrum into three different spectra range of (a) 1300-1900 cm^{-1} , (b) 1800-2400 cm^{-1} and (c) 2600-3800 cm^{-1} .	73

Figure 3.19	Example of the deconvolution of FTIR spectra using Gaussian fitting for the spectra range of (a) 1000-2000 cm^{-1} , (b) 2000-2300 cm^{-1} and (c) 2700-3200 cm^{-1} . Also shown are the peak positions for the functional groups of interest.	74
Figure 3.20	FEI Quanta 200 field emission scanning electron (FESEM) microscope used for surface and cross-sectional high resolution imaging of carbon nitride films.	76
Figure 3.21	JEOL JEM-2100F high resolution transmission electron microscope used for high resolution imaging of individual nanostructured carbon nitride strands, energy dispersive x-ray (EDX) and selected area electron diffraction (SAED) analysis.	77
Figure 4.1	Variation of FESEM surface and cross-sectional images spectra for films deposited as a function of electrode distance.	80
Figure 4.2	Variation of FESEM surface images for films deposited at electrode distance of (a) 6 cm, (b) 3 cm, (c) 2 cm and (d) 1 cm	81
Figure 4.3	Variation of FESEM surface images for films deposited at electrode distance of 6, 3, 2 and 1 cm.	81
Figure 4.4	Variation in growth rate for the thin films and nanostructures calculated from the FESEM cross-sectional images, spectra for films deposited as a function of electrode distance. Lines are as guide to the eyes.	82
Figure 4.5	FESEM surface image of films grown on silicon substrate from pure CH_4 (a) and (b), mixture of CH_4 and H_2 (c) and mixture of CH_4 and Ar (d) gasses. Image (b) is the higher magnification image of (a) shown for clarification.	84
Figure 4.6	Variation in AES spectra for films deposited as function of electrode distance.	86
Figure 4.7	Variation of nitrogen to carbon N/C ratio spectra for films deposited as a function of electrode distance.	87
Figure 4.8	Variation in Raman scattering spectra for films deposited as a function of electrode distance, whereby (a) shows the raw data obtained with a significant decrease in photoluminescence background with decrease in electrode distance, and (b) shows the deconvolution of the Raman spectra after photoluminescence background extraction.	89
Figure 4.9	Gaussian fitting results for films deposited as a function of electrode distance	90
Figure 4.10	Variation in FTIR absorbance spectra for films deposited as a function of electrode distance in the range of 1000 - 4000 cm^{-1} .	94

Figure 4.11	Variation in FTIR absorbance spectra for films deposited as a function of electrode distance in the range of (a) sp^2 , (b) sp^1 and (c) sp^3 phases.	95
Figure 4.12	Variation in FTIR absorbance spectra for films deposited as a function of electrode distance in the range of 1900-2300 cm^{-1} for the $C\equiv N$ region.	96
Figure 4.13	Gaussian fitting profiles for the FTIR spectra in the region of 1900-2300 cm^{-1} for the electrode distance of (a) 1cm, (b) 2cm and (c) 6cm. The blue line show the Gaussian fitting for the spectra (black points) and the red line shows the overall fitting curve.	97
Figure 4.14	FESEM surface image of nanostructures grown on quartz substrate. Part of the film was intentionally scratched to expose the cross-sectional view of the nanostructures.	99
Figure 4.15	Variation in optical energy gap for films deposited as a function of electrode distance. Line is drawn as guide for the eye.	100
Figure 4.16	Variation in optical energy gap for films deposited as a function of electrode distance. Line is drawn as guide for the eye.	102
Figure 4.17	Gaussian fitting profiles for the PL spectra for D_E of 6 to 2 cm. for the electrode distance of (a) 1cm, (b) 2cm and (c) 6cm. The blue line show the Gaussian fitting for the spectra (black points) and the red line shows the overall fitting curve.	104
Figure 4.18	Variation in integrated PL intensities as a function of electrode distance. Line is drawn as guide for the eye.	104
Figure 5.1	Schematic diagram of densification by subplantation (Robertson 2002a)	113
Figure 5.2	Schematic of the penetration and relaxation stage for cases of single and molecular impinging ions (Robertson 2002a).	113
Figure 5.3	Flow chart showing the progression of the current studies of $p-CN_x:H$ films	116
Figure 5.4	Variation of growth rate as a function of applied rf power. Line is as guide to the eye.	118
Figure 5.5	Variation of optical energy gap (\square) and refractive index (\blacklozenge) as a function of applied rf power. Line is as guide to the eye.	119
Figure 5.6	Variation in photoluminescence as a function of applied rf power.	120

Figure 5.7	Example of photoluminescence Gaussian fitting for the film deposited at applied rf power of 80W.	120
Figure 5.8	Variations of the peak intensities and positions at the photon emission range of (a) 2.48-2.69 and (b) 3.03-3.10 eV for films deposited as a function of applied rf power.	121
Figure 5.9	Variations of the peak intensities and positions at the photon emission range of (a) 2.48-2.69 and (b) 3.03-3.10 eV for films deposited as a function of applied rf power. Lines are as guide to the eyes.	123
Figure 5.10	Variation of nitrogen to carbon N/C ratio for films deposited as a function of applied rf power.	124
Figure 5.11	Variation in Raman scattering spectra for films deposited as a function of applied rf power, whereby (a) shows the raw data and (b) shows the deconvolution of the Raman spectra after photoluminescence background extraction.	126
Figure 5.12	Variation in FTIR absorbance spectra for films deposited as a function of applied rf power in the range of 1000-4000 cm^{-1} .	128
Figure 5.13	Variation in FTIR absorbance spectra for films deposited as a function of applied rf power in the range of (a) sp^2 , (b) sp^1 and (c) sp^3 phases.	129
Figure 5.14	Variation in sp^2 , sp^3 and sp^2/sp^3 ratio for films deposited as a function of applied rf power.	130
Figure 5.15	Variation in (a) C=C, C=N and/or N-H absorbance peaks and (b) various nitrile and isonitrile absorbance peaks for p-CN _x :H films deposited as a function of applied rf power.	132
Figure 5.16	Flow chart showing the progression of the current studies of p-CN _x :H films.	134
Figure 5.17	Variation of growth rate for p-CN _x :H films deposited as a function of nitrogen-to-methane gas flow-rate ratio. Line is as guide to the eye.	135
Figure 5.18	Variation of optical energy gap (\square) and refractive index (\blacklozenge) for p-CN _x :H films deposited as a function of nitrogen-to-methane gas flow-rate ratio. Lines are as guide to the eye.	136
Figure 5.19	Variation in photoluminescence spectra for p-CN _x :H films deposited as a function of nitrogen-to-methane flow-rate ratio. Inset show enlarged selected spectra for ratio of 0, 0.4-0.5 and 0.8-0.9 for further clarification.	137
Figure 5.20	Variations of the peak intensities and positions at the photon emission range of (a) 2.45-2.56 and (b) 3.03-3.10 eV for p-CN _x :H films deposited as a function of nitrogen-to-methane	138

	flow-rate ratio. Lines are as guide to the eyes.	
Figure 5.21	Variation of nitrogen to carbon N/C ratio for p-CN _x :H films deposited as a function of nitrogen-to-methane flow-rate ratio. Line is as guide to the eye.	139
Figure 5.22	Variation in Raman scattering spectra for p-CN _x :H films deposited as a function of nitrogen-to-methane flow-rate ratio, whereby (a) shows the raw data and (b) shows the deconvolution of the Raman spectra after photoluminescence background extraction.	141
Figure 5.23	Variation in FTIR absorbance spectra for p-CN _x :H films deposited as a function of nitrogen-to-methane flow-rate ratio in the range of 1000-4000 cm ⁻¹ .	142
Figure 5.24	Variation in FTIR absorbance spectra for p-CN _x :H films deposited as a function of of nitrogen-to-methane flow-rate ratio in the range of (a) sp ² , (b) sp ¹ and (c) sp ³ phases.	143
Figure 5.25	FTIR spectra in the region of 1100-1900 cm ⁻¹ showing the variation in the N-H, C=C and/or C=N bonds for p-CN _x :H films deposited as a function of of nitrogen-to-methane flow-rate ratio.	146
Figure 5.26	Variation in (a) C=C and/or C=N and (b) various nitrile and isonitrile absorbance peaks for p-CN _x :H films deposited as a function of nitrogen-to-methane flow-rate ratio. Line is as guide to the eye.	147
Figure 5.27	Flow chart showing the progression of the current studies of p-CN _x :H films.	151
Figure 5.28	Variation of film thickness as a function of annealing temperature. Line is as guide to the eye.	152
Figure 5.29	Variation in FTIR absorbance spectra as a function of annealing temperature in the range of 1000-4000 cm ⁻¹ .	153
Figure 5.30	Variation in FTIR absorbance spectra as a function of annealing temperature in the range of (a) sp ² , (b) sp ¹ and (c) sp ³ phases.	154
Figure 5.31	Variation in absorbance intensities of various FTIR deconvoluted peaks including (a) C=C and/or C=N, sp ³ CH _x and N-H, (b) various nitrile and isonitrile bonds, and (c) various CH _n bonds for p-CN _x :H films as a function of annealing temperature. Lines are as guide to the eye.	156
Figure 5.32	Variation of optical energy gap as a function of annealing temperature. Line is as guide to the eye.	158

Figure 5.33	Variation of nitrogen to carbon, N/C ratio as a function of annealing temperature. Line is as guide to the eye.	160
Figure 5.34	Variation in Raman scattering spectra as a function of annealing temperature, whereby (a) shows the raw data and (b) shows the deconvolution of the Raman spectra after photoluminescence background extraction.	161
Figure 5.35	Variations in (a) peak position and width of D band, and (b) I_D/I_G , as a function of annealing temperature. Lines are as guide to the eye.	162
Figure 5.36	Variation in photoluminescence spectra as a function of annealing temperature. Inset show enlarged selected spectra for the annealing temperature of 500 °C and 700 °C shown for further clarification.	164
Figure 5.37	Variations of the peak intensities and positions at the photon emission range of (a) 2.45-2.56 with relation to sp^2 clustering and (b) 3.03-3.10 eV with relation to nitrogen bonding as a function of annealing temperature. Lines are as guide to the eyes.	165
Figure 6.1	Flow chart showing the progression of this current section	171
Figure 6.2	Variation of FESEM surface and cross-sectional images for films deposited as a function of applied rf power.	173
Figure 6.3	Enlarged FESEM surface and cross-sectional images of ns-CN _x :H films for films deposited at various applied rf power.	174
Figure 6.4	Variation in diameter and length of CN _x :H nanostructures deposited as a function of applied rf power.	175
Figure 6.5	Variation of nitrogen to carbon N/C ratio for films deposited as a function of applied rf power.	177
Figure 6.6	Variation in Raman scattering spectra for films deposited as a function of applied rf power, whereby (a) shows the raw data obtained and (b) shows the deconvolution of the Raman spectra after photoluminescence background extraction.	178
Figure 6.7	Gaussian fitting variation for peak position and full width half maximum for G-band, (a) and (b), respectively, and D band, (c) and (d), respectively, and the corresponding I_D/I_G ratio, (e).	179
Figure 6.8	Variation in FTIR absorbance spectra for films deposited as a function of applied rf power in the range of 1000-4000 cm^{-1} .	181
Figure 6.9	Variation in FTIR absorbance spectra for films deposited as a function of applied rf power for (a) sp^2 , (b) sp^1 and (c) sp^3 phases.	182

Figure 6.10	Gaussian fitting profiles for the FTIR spectra in the region of 1900-2300 cm^{-1} for films deposited as a function of applied rf power. The blue line show the Gaussian fitting for the spectra (black points) and the red line shows the overall fitting curve.	183
Figure 6.11	FESEM images for ns-CN _x :H deposited at applied rf power of 100 W showing (a) the “root”, middle and “tip” sections of the fibers and (b) the enlarged image of the “root” sections.	186
Figure 6.12	Flow chart showing the progression of this current section	188
Figure 6.13	Variation of FESEM surface and cross-sectional images for films deposited as a function of nitrogen-to-methane gas flow-rate ratio calculated as $[\text{N}_2/(\text{N}_2+\text{CH}_4)]$. Images are taken at two different magnification factors.	191
Figure 6.14	Cross-sectional images taken for the formation of vertically aligned nanostructures at $[\text{N}_2/(\text{N}_2+\text{CH}_4)]$ of (a) 0.70 and (b) 0.75. Note that images are shown at different magnification factors chosen for clarification.	191
Figure 6.15	Variation of nitrogen to carbon N/C ratio for films deposited as a function of nitrogen-to-methane gas flow-rate ratio calculated as $[\text{N}_2/(\text{N}_2+\text{CH}_4)]$.	192
Figure 6.16	Variation in Raman scattering spectra for films deposited as a function of nitrogen-to-methane gas flow-rate ratio calculated as $[\text{N}_2/(\text{N}_2+\text{CH}_4)]$, whereby (a) shows the raw data obtained and (b) shows the deconvolution of the Raman spectra after background extraction.	194
Figure 6.17	Raman Gaussian fitting for films deposited as a function of nitrogen-to-methane gas flow-rate ratio for peak position and full width half maximum for G-band, (a) and (b), respectively, and D band, (c) and (d), respectively, and the corresponding I_D/I_G ratio, (e).	195
Figure 6.18	Variation in FTIR absorbance spectra for films deposited as a function of nitrogen-to-methane gas flow-rate ratio in the range of 1000-4000 cm^{-1} .	197
Figure 6.19	Variation in FTIR absorbance spectra for films deposited as a function of nitrogen-to-methane gas flow-rate ratio in the range of (a) sp^2 , (b) sp^1 and (c) sp^3 phases.	198
Figure 6.20	Gaussian fitting profiles for the FTIR spectra in the region of 1900-2300 cm^{-1} as a function of nitrogen-to-methane gas flow-rate ratio. The blue line show the Gaussian fitting for the spectra (black points) and the red line shows the overall fitting curve.	199

Figure 6.21	Comparison of FESEM surface images and FTIR spectra for (a) ns-N _x :H, (b) non-nitrogenated C:H and (c) p-CN _x :H films.	202
Figure 6.22	Flow chart showing the progression of this current section	203
Figure 6.23	Variation of FESEM surface and cross-sectional images of ns-CN _x :H films deposited as a function of deposition duration. Images are taken at two different magnification factors.	205
Figure 6.24	Variation in diameter and length of ns-CN _x :H films deposited as a function of deposition duration. Lines are as guide to the eye.	207
Figure 6.25	Variation in AES spectra of the ns-CN _x :H films deposited as a function of deposition duration	208
Figure 6.26	Variation of nitrogen to carbon N/C ratio of the ns-CN _x :H films deposited as a function of deposition duration	208
Figure 6.27	Variation in Raman scattering spectra of the ns-CN _x :H films deposited as a function of deposition duration, whereby (a) shows the raw spectra, and (b) shows the deconvolution of the Raman spectra after photoluminescence background elimination.	210
Figure 6.28	Raman Gaussian fitting trends for peak position and full width half maximum for G-band, (a) and (b), respectively, and D band, (c) and (d), respectively, and the corresponding I _D /I _G ratio, (e).	211
Figure 6.29	Variation in FTIR absorbance spectra of the ns-CN _x :H films deposited as a function of deposition duration in the range of 1000-4000 cm ⁻¹ .	213
Figure 6.30	Variation in FTIR absorbance spectra of the ns-CN _x :H films deposited as a function of deposition duration in the range of (a) sp ² , (b) sp ¹ and (c) sp ³ phases.	214
Figure 6.31	Gaussian fitting profiles for the FTIR spectra in the region of 1900-2300 cm ⁻¹ of the ns-CN _x :H films deposited as a function of deposition duration. The blue line show the Gaussian fitting for the spectra (black points) and the red line shows the overall fitting curve.	215
Figure 6.32	High resolution TEM at varied magnification for the upper tip of the nanostructures formed for the deposition duration of 75 minutes (a)-(e). (f) and (i) are the SAED pattern obtained for the nanocrystallite cluster and amorphous components. (g) and (h) shows the atomic resolution images and EDX spectrum of the crystallites.	218
Figure 6.33	Schematic illustration of the proposed growth mechanism for the vertically aligned CN _x :H nanorods .	219

Figure A1	The home-built rf PECVD system employing parallel plate electrodes for the fabrication of the polymeric and nanostructured carbon nitride films in this work.	244
Figure A2	Various trends in bonding and structural characteristics calculated from the Gaussian fittings of FTIR spectra for different deposition parameters at different spectra range. Also included are their corresponding AES N/C and PL results.	245

LIST OF TABLES

	page
Table 2.1 List of bonding assignments wavenumber regions and corresponding references.	43
Table 3.1 Deposition parameters for the study of the effects of electrode distance on the structural properties of $CN_x:H$ thin films.	57
Table 4.1 Deposition parameters for the study of the effects of electrode distance on the structural properties of $CN_x:H$ thin films.	79
Table 5.1 Deposition parameters for the study of the effects of applied rf power on the structural properties of $CN_x:H$ thin films.	117
Table 5.2 Raman fitting parameter fro film deposited as a function of applied rf power.	125
Table 5.3 Deposition parameters for the study of the effects of nitrogen-to-methane gas flow-rate ratio on the properties of $CN_x:H$ thin films.	133
Table 6.1 Deposition parameters for the study of the effects of electrode distance on the structural properties of $CN_x:H$ thin films.	172
Table 6.2 Deposition parameters for the study of the effects of nitrogen-to-methane gas flow-rate ratio on the properties of $CN_x:H$ thin films.	189
Table 6.3 Deposition parameters for the study of the effects of deposition duration on the growth of ns- $CN_x:H$ thin films.	204